2022-06-07

Modeling Inter-Particle Magnetic Correlations in Magnetite Nanoparticle Assemblies Using X-ray Magnetic Scattering Data

Johnathon Michael Rackham
Brigham Young University

Modeling Inter-Particle Magnetic Correlations in Magnetite Nanoparticle Assemblies Using X-ray Magnetic Scattering Data

Johnathon Michael Rackham

A thesis submitted to the faculty of
Brigham Young University
in partial fulfillment of the requirements for the degree of

Master of Science

Karine Chesnel, Chair
Mark Transtrum
Branton Campbell

Department of Physics and Astronomy

Brigham Young University

ABSTRACT

Modeling Inter-Particle Magnetic Correlations in Magnetite Nanoparticle Assemblies Using X-ray Magnetic Scattering Data

Johnathon Michael Rackham
Department of Physics and Astronomy, BYU
Master of Science

Magnetic nanoparticles are used in nanotechnologies and biomedical applications, such as drug targeting, hyperthermia, MRI contrasting agents, and bio-separation of compound solutions. Magnetite (Fe_3O_4) nanoparticles stand to be effective in these roles due to the non-toxic nature of magnetite and its ease of manufacture. To this end, a greater understanding of the magnetic behavior of the individual magnetite nanoparticles is needed when a collection of them is used. This research seeks to discover the local magnetic ordering of ensembles of magnetite nanoparticles at various stages of the magnetization process, temperatures above and below their blocking temperature, and for various particle sizes. We use x-ray circular dichroism and x-ray resonant magnetic scattering (XRMS), which provides information about the magnetic orders in the samples. Here we discuss the modeling of the magnetic scattering data using a one-dimensional chain of nanoparticles in real space as well as an empirical Gaussian packet model in reciprocal space. We find that at low temperature, and field values close to the coercive point, magnetite nanoparticles experience a significant amount of antiferromagnetic ordering that increases with particle size.

Keywords: magnetite, nanoparticles, magnetic scattering, XRMS, computational modeling

ACKNOWLEDGMENTS

I would like to thank the diligent guidance of my advisory committee, Dr. Karine Chesnel, Dr. Mark Transtrum, and Dr. Branton Campbell. Additionally, the support of BYU Physics department, and the bottomless patience of my family and friends were invaluable. I would not have made it this far without all of you.

Contents

Table of Contents **iv**

1 Introduction and Background **1**
1.1 Motivation 1
1.2 Prior Work 2
1.3 Statement Problem and Thesis 3

2 Sample and Data Preparation **4**
2.1 Characterization of Samples 4
2.2 XMCD and XRMS Diffraction Images 6
2.2.1 Preparation of Data 7

3 Models **10**
3.1 Formulation 10
3.1.1 1D Nanoparticle Chains 11
3.1.2 Empirical Gaussian Fit 15
3.2 Parameter Optimization Methods 17
3.2.1 Levenberg-Marquardt 17
3.2.2 Basin Hopping 17

4 Results and Analysis **18**
4.1 Fisher Information Matrix 18
4.2 Profile Likelihood 19
4.3 Model Results 20
4.3.1 Nanochain Model 21
4.3.2 Empirical Gaussian Fit 24

5 Conclusion **30**

Appendix A Magnetic Ratio Derivation **31**

Bibliography **35**

Chapter 1

Introduction and Background

1.1 Motivation

Magnetic nanoparticles (NPs) are quickly becoming an integral part of many industries such as biomedicine, computer hardware, and even the automotive industry [1]. The biomedical industry is exploring the use of magnetic NPs in various applications such as MRI contrasting agents, but also for additional use in drug targeting, hyperthermia, and bio-separation [2–4]. Also, computer systems rely on data storage and magnetic NPs could provide a better way to manufacture long term high density magnetic storage media [5]. Additionally, the engineers of suspension systems in high performance vehicles are also exploring the use of magnetic NPs to dynamically alter the viscosity of shock absorber dampening fluids [6].

Magnetite (Fe_3O_4) is a commonly occurring ferromagnetic iron oxide found in many minerals, which makes it an ideal candidate for the applications mentioned above because of its non-toxic nature and how easy it is to manufacture at scale. Successfully optimizing the use of magnetite NPs for use these applications, and many others, could lead to breakthroughs in cancer diagnosis and treatment, faster computers, and safer vehicles. However, in order to accomplish this we need

a greater understanding of how assemblies of magnetite NPs behave while exposed to external magnetic fields.

The properties of bulk materials are largely determined by the arrangement of the atoms that make up their composition. Because of the greater ratio of surface area to volume, NPs potentially exhibit properties that differ from the material in bulk form. We are primarily concerned with the properties that express on the nanoscale. In particular, the particle size, how easily NPs self-assemble into regular arrangements, and how the nanospin moments behave.

The behavior of nanospin moments gives rise to a unique magnetic phase called superparamagnetism which is the tendency of sufficiently small particles to randomly flip nanospin orientation due to thermal activation. However, if the temperature is small there is not enough thermal energy for the random flip to occur within typically measured time frames and the particle is considered magnetically blocked. The temperature at which this occurs is the blocking temperature (T_B). The existing magnetic correlations and the dynamics of magnetic fluctuation are some of the characteristics traits of NP assemblies that needs to be understood. To this end, we are employing several methods of probing the characteristics of NPs to determine the necessary information for improving the application of magnetite NPs.

1.2 Prior Work

Magnetite's bulk properties are well established [7]. Because of the rising interest in the material in its nanoparticle form, recent research has focused on probing the magnetic properties of collections of NP, which may be in the form of a powder or thin monolayered assembly [8]. The particular samples we examine in this work were fabricated at Brigham Young University (BYU) using an organic solution method. The characterization of these samples begins with x-ray diffraction (XRD). The XRD measurements reveal that the spectrum of individual particles is consistent with the

crystal structure of bulk magnetite [8], as shown in Figure 2.1. Additionally, transmission electron microscopy (TEM) images were used to determine the distribution of particle sizes present in the samples and example images are also shown in Figure 2.1. The collective magnetic behavior of the samples was determined using vibrating sample magnetometry (VSM). The magnetization loops measured at various temperatures showed a smooth Langevin-type shape, characteristic of superparamagnetic behavior at high temperatures [9]. Zero-Field-Cooling (ZFC) and Field Cooling (FC) curves also indicated superparamagnetic behavior with blocking temperatures that are directly correlated to the size of NPs [10]. The prior work done on this topic suggests that for larger particles there may be inter-particle coupling at low external field values that could cause interesting magnetic ordering within the ensembles of NPs. To determine the orbital and spin contributions to the magnetic moment of our Fe_3O_4 NPs we used x-ray magnetic circular dichroism (XMCD). Furthermore, to probe the nanoscale magnetic correlations we used x-ray resonant magnetic scattering (XRMS)

1.3 Statement Problem and Thesis

A more detailed accounting of these characteristics, specifically for the 5 and 11 nm Fe_3O_4 NPs examined by this work, is reported in this thesis. In particular, what we thoroughly explored is the behavior of magnetite NP assemblies when exposed to the external magnetic fields that the applications mentioned above potentially require. This work seeks to discover and characterize the local magnetic ordering of magnetite NP assemblies using XRMS data collected at synchrotron facilities and a modeling process in both real and reciprocal space.

Chapter 2

Sample and Data Preparation

2.1 Characterization of Samples

This work examines magnetite NP assemblies of two particle diameters, one of 5 nm and another of 11 nm. These samples were prepared in collaboration with Dr. Roger Harrison of the Brigham Young University Chemistry Department. The exact procedure used to manufacture the NPs can be found here [8, 10, 11]. As mentioned above the NP characteristics were previously determined in our lab on campus via XRD, TEM, and VSM. The TEM imaging and ZFC/FC results are of particular interest here and later informed the parameters used in the modeling processes including the temperature and field values the data was collected at. The TEM images, shown in Fig. 2.1, show that the 5 nm diameter NP assemblies are more homogeneous in size than the 11 nm NP assemblies. This homogeneity leads to more closely packed arrangements (as seen on the TEM images). The FC and ZFC measurements were taken by cooling the sample in the presence of an external field (FC), or without a field presence (ZFC), respectively. The magnetization is then tracked as the temperature of the sample is increased. Larger diameter NPs have higher blocking temperatures (T_B) compared to smaller particles: precisely $T_B = 25$ K for the 5 nm NP whereas $T_B \sim 170$ K for 11 nm

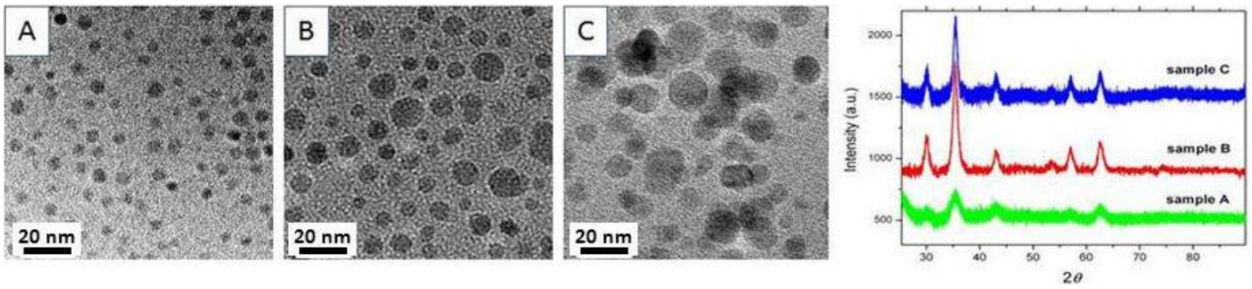

Figure 2.1 TEM images and XRD patterns of the Fe_3O_4 nanoparticles (A) 5 nm (B) 8 nm (C) 11nm. Extracted from [10].

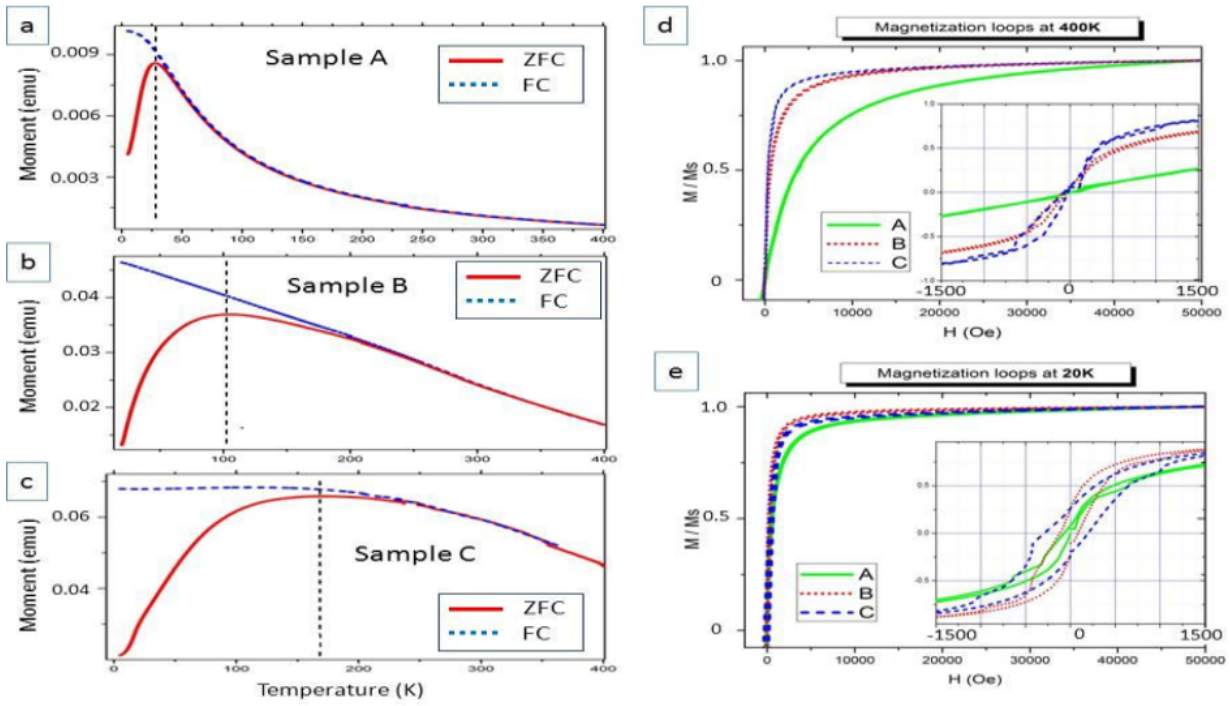

Figure 2.2 (a-c) ZFC/FC measurements of sample A (5 nm), B (8 nm), and C (11 nm) measured at 100 Oe. (d) Magnetization curves, measured at 400 K and (e) at 20 K. Insets: close-up on hysteresis extracted from [10].

NPs. When below the blocking temperature, the particles remain magnetically frozen and do not have enough thermal energy for the nanospin moment to flip in a typical observation timescale [10].

The VSM magnetization loops define the saturation and coercive points for each sample, and the hysteresis exhibited at low applied field values gives an indication of some manner of inter particle coupling. This coupling could result in interesting magnetic ordering in the samples. The following table comprises a summary of the characteristic quantities for the samples used in this work.

Sample	NP5	NP11
Average Diameter	5 nm	11 nm
Diameter Variance	$\pm$0.7 nm	$\pm$2.5 nm
Blocking Temperature	25 K	$\sim$ 170 K
M_{3000}/M_s at 300 K	0.575	0.908
M_{3000}/M_s at 20 K	0.829	0.899
H_c at 300 K	0 Oe	0 Oe
H_c at 20 K	0 Oe	-300 Oe

Table 2.1 Summary of magnetic sample characteristics determined by VSM magnetometry and TEM images. M_{3000}/M_s is the ratio of the magnetization taken at field value of 3000 Oe and the magnetization at saturation. H_c is the coercive point. Data extracted from TEM, XRD, VSM measurements carried at BYU by the Chesnel group.

2.2 XMCD and XRMS Diffraction Images

In addition to the magnetic characterization detailed above, the bulk of the data used in this work is comprised of x-ray resonant magnetic scattering (XMRS) diffraction images. These XRMS images were collected at opposite helicities of circular polarized light whose energy was tuned to the L_3 resonant edge of Fe for magneto-optical contrast. These data were collected at the Stanford Synchrotron Radiation Lightsource with an optical setup detailed here [12]. When the x-ray energy is tuned to a resonant edge it provides necessary magneto-optical contrast to provide magnetic scattering information. Additionally, the use of partially coherent x-ray light leads to coherent

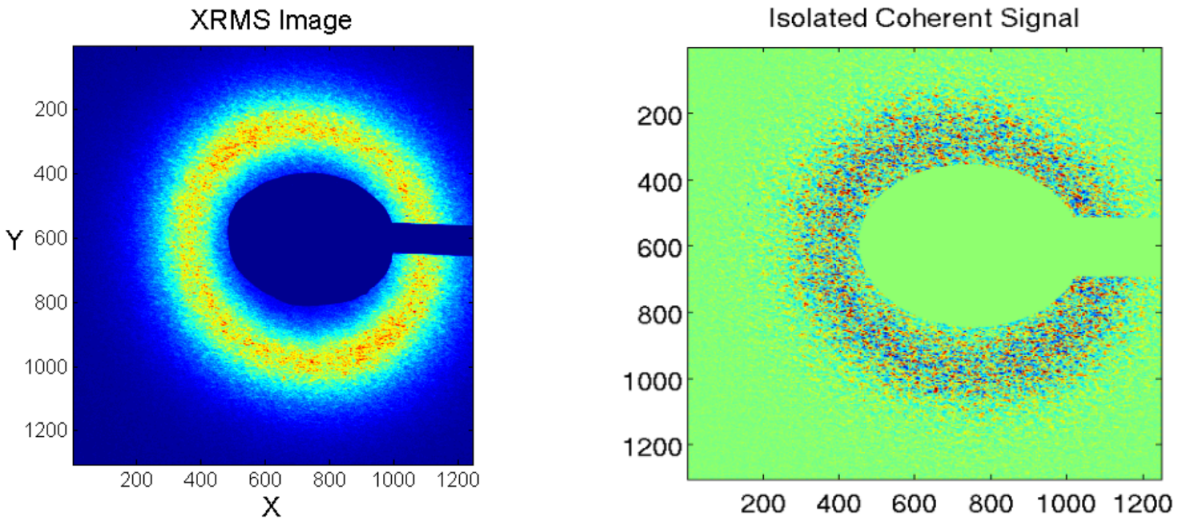

(a) **(b)**

Figure 2.3 (a) Example of an XRMS diffraction pattern. (b) Resulting speckle pattern after extracting the coherent signal extracted from [9].

scattering in the form of a speckle pattern. The speckle pattern found in the coherent portion of the diffraction images constitutes a unique fingerprint of the magnetic ordering in real space at the time of illumination. By examining changes in the diffraction images it is possible to extract information about the local magnetic ordering as a function of temperature and applied field for a given particle size. Figure 2.3 shows example diffraction images and the resulting speckle pattern. However, in this thesis work, we did not focus on the speckle patterns themselves, but instead we utilized signals constructed from the images in a manner detailed below.

2.2.1 Preparation of Data

We use the XRMS speckle patterns to construct 1D signals by first integrating them azimuthally and then examining the changes between data collected at opposite helicities of the incident x-ray light. To reduce the 2D diffraction images we angularly integrate around the center of the diffraction ring to project the signal into 1D. To separate the charge scattering signal from the magnetic scattering

signal we compare signals collected at opposite helicities of the light, $I+$ and $I-$. The charge scattering signal is estimated via the sum $I_c = I^+ + I^-$. The magnetic ratio

$$R_m = \frac{I^+ - I^-}{\sqrt{I^+ + I^-}}$$

derived in appendix A, gives us information about the magnetic scattering signal from which we hope to extract information on magnetic ordering. Due to variances in the incident beamline intensity, thermal drift, and other factors outside of experimental control, it is difficult to directly compare the absolute magnitude of I_c and R_m. Here we focus essentially on their dependence with the scattering vector q, which has the most important information about magnetic ordering. To make comparison at various fields and temperatures possible, we normalize the signals at the maximum value of the main peak at position q^* as shown in Figure 2.4 where we provide examples of the NP11 sample data. The shape of the charge scattering signals does not significantly vary when an external magnetic field is applied and changed in magnitude. This indicates that the NPs in the assemblies are not physically moving around on the mounting substrate as an external magnetic field is applied. The interesting features are found in the way the magnetic scattering ratio R_m changes with the applied field. Panel (b) of Figure 2.4 shows the shape of the R_m drastically changing with the external field H in particular at $q^*/2$. Next, we discuss the formulation of the models used to recreate R_m and extract information about magnetic correlations from it.

(a)

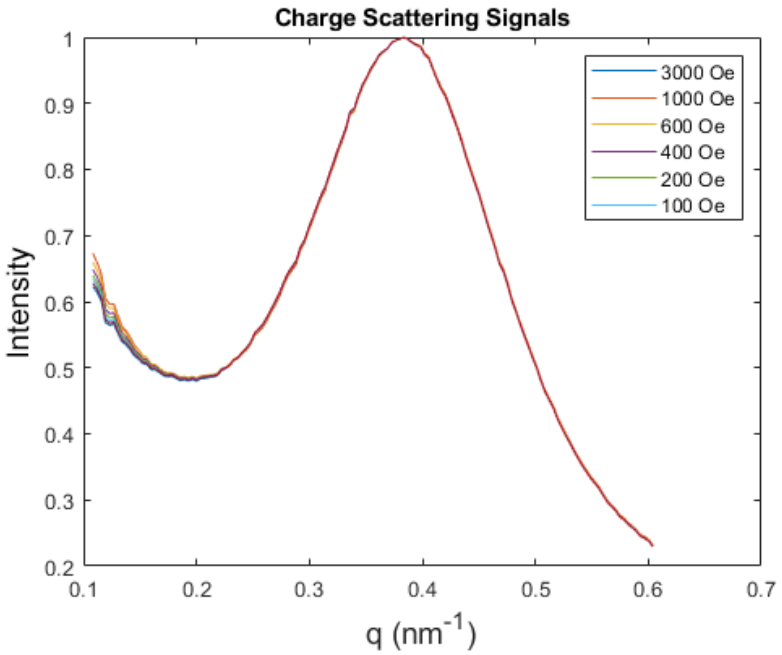

(b)

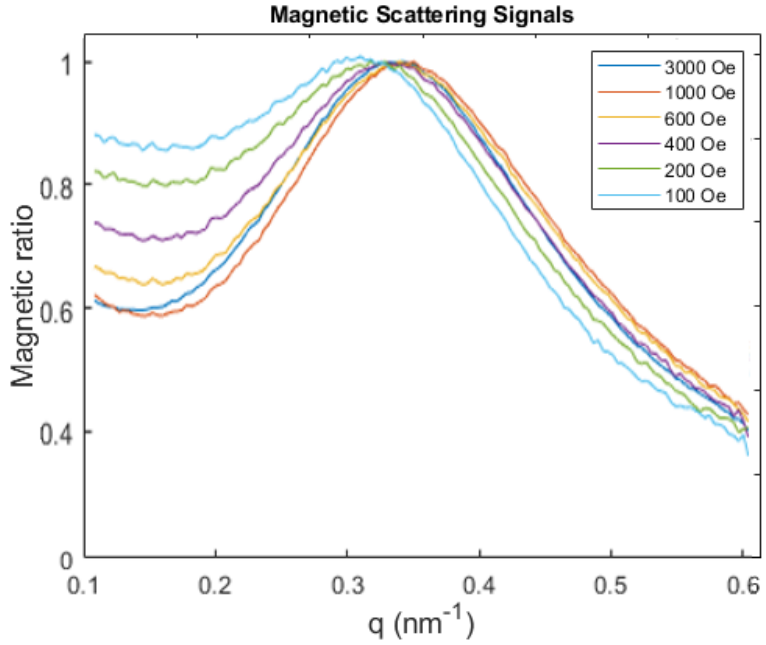

Figure 2.4 Data collected from the 11 nm sample at 300 K with applied field values ranging from 100 to 3000 Oe. (a) The charge scattering signals (b) Magnetic Scattering signals found with the magnetic ratio.

Chapter 3

Models

3.1 Formulation

Predictive models typically fall on a point somewhere along the axis spanning from a purely mechanistic to purely empirical formulation. On one hand, mechanistic models seek to describe phenomena based on deterministic physical laws expressed as derivations of independent variables. On the other hand, empirical models make no attempt to use physical laws to explain phenomena, but instead only fit observed data and utilize extrapolation or interpolation to predict outcomes. This work examines the behavior of magnetite NP assemblies through both a mechanistic simulation of particle assemblies in real space and through an empirical fitting process of the XRMS data collected in reciprocal space.

As mentioned in section 2.2 the number of particles illuminated by the x-ray beam is sufficiently large (in the order of millions) to make direct simulation computationally impossible. In order to model the magnetic behavior of the NP assemblies we make two main simplifications so the problem becomes tractable. The first assumption is that the physics governing the NP interactions can largely be captured by using a 1D representation of the NP assembly as a chain of spherical particles.

Given the high number of NPs illuminated, which averages the multiple lattice orientations, the 2D magnetic correlations function is nearly isotropic and its radial part can therefore be represented by a 1D model. Second, we assume that the lengths associated to the various magnetic correlations die off rapidly enough to ensure that these chains can be finite in length. We account for the variance in particle spacing and diameter present in the samples by averaging multiple chain models together before Fourier transforming the resulting charge density function and comparing the result to the data that was shown in section 2.2.1.

3.1.1 1D Nanoparticle Chains

We begin the modeling process by constructing 1D chains of spherical NPs using a particle diameter and spacing estimated from the distributions measured from the TEM images of the samples shown in Table 2.1 and illustrated in figure 3.1. With these values, the 3D charge density function (CDF) we project spheres of the given diameters and spacing into a 1D CDF as illustrated in Figure 3.2a. We then construct and average ten additional chains, each with values uniformly sampled from the observed distribution of particle diameters and spacing. The weighted summation of this collection of 1D chains serves as the representation of the NP assembly in real space. The resulting average CDF is then a function of position r and fitting parameters, $\boldsymbol{\theta}$, and takes the form

$$C(\boldsymbol{\theta};r) = \sum_i P(i)\phi_i(\boldsymbol{\theta};r) \tag{3.1}$$

where ϕ_i is the 1D chain for a given diameter and spacing. $P(i)$ is the probability of that chain occurring based on the observed distribution of particle size and spacing measured from the TEM images discussed in Section 2.1. $\boldsymbol{\theta}$ is a vector of parameters used in the model and fitting methods described in chapter 4.

From the chains used to construct the CDF we create "magnetic density functions" (MDF) representing various magnetic orders, including ferromagnetic (FM) and anti-ferromagnetic ordering

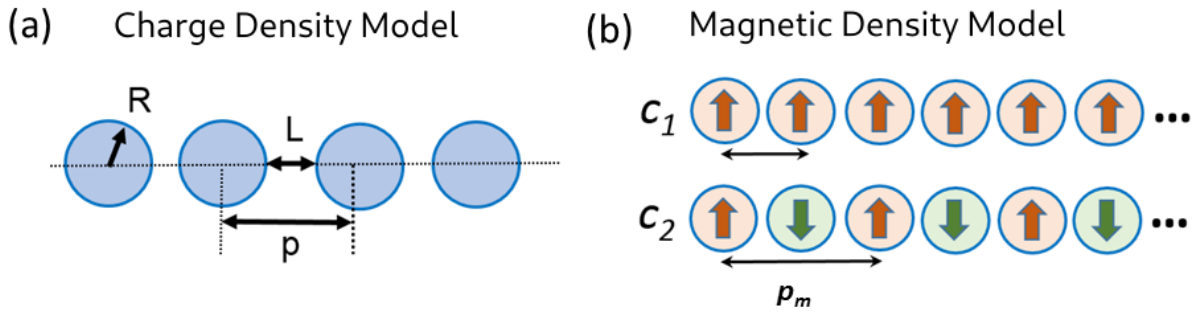

Figure 3.1 (a) Illustration of charge density chains using particle radius(R), period (p) and particle spacing (L). (b) Illustration magnetic NP chains exhibiting AF and FM ordering [13]

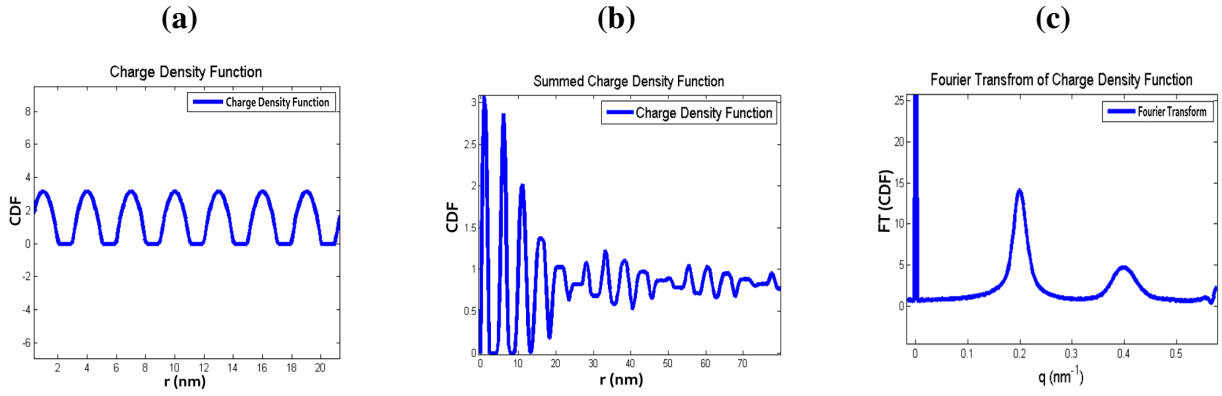

Figure 3.2 (a) Charge density function representing a chain of spherical NP of specific diameter and spacing into 1D. (b) Summed charge density function. (c) Fourier Transform of charge density function

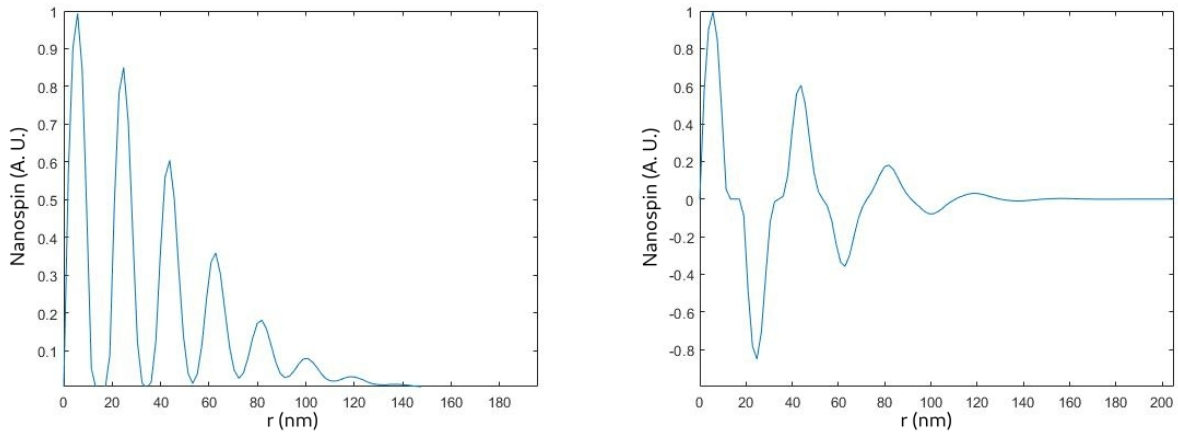

(a) Ferromagnetic MDF Chain **(b)** Anti-ferromagnetic MDF Chain

Figure 3.3 Examples of magnetic order chains convoluted with a Gaussian function to determine correlations

(AF), by assigning the corresponding spin values to each particle site in the chain. The convolution of a Gaussian function centered at $r = 0$ and the MDF accounts for magnetic correlation lengths as shown in figure 3.3.

The resulting MDF for the FM and AF ordering are respectively:

$$FM(\boldsymbol{\theta};r) = \sum_i S_{FM,i}(r)\, P(i)\, \phi_i(\boldsymbol{\theta};r)\, \mathscr{N}_{FM}(\boldsymbol{\theta};r) \tag{3.2}$$

$$AF(\boldsymbol{\theta};r) = \sum_i S_{AF,i}(r)\, P(i)\, \phi_i(\boldsymbol{\theta};r)\, \mathscr{N}_{AF}(\boldsymbol{\theta};r) \tag{3.3}$$

Equations 3.2-3 describe these spin chains with $\mathscr{N}$ being the normal Gaussian functions for the respective FM and AF correlations and $S_{FM,i}$ and $S_{AF,i}$ are functions containing the corresponding spin values.

We then form the overall magnetic density function $M(\theta;r)$ from a linear combination of the FM and AF functions as follows

$$M(\boldsymbol{\theta};r) = c_1\, FM(\boldsymbol{\theta};r) + c_2\, AF(\boldsymbol{\theta};r)$$

where c_1 and c_2 are the weighing coefficients for the linear combination of FM and AF orders in the

Parameter	Description
θ_1	mean particle separation (L_0)
θ_2	charge signal offset
θ_3	magnetic signal offset
θ_4	AF component(c_2)
θ_5	charge peak magnitude
θ_6	magnetic central (q=0) peak height
θ_7	charge central (q=0) peak height
θ_8	FM correlation length (σ_{FM})
θ_9	AF correlation length (σ_{AF})
θ_{10}	Charge peak width
θ_{11}	magnetic central (q=0) width
θ_{12}	charge central (q=0) peak width

Table 3.1 Description of the parameters used in the nano chain model

mix and are contained in the parameter vector $\boldsymbol{\theta}$. A full detailing of the parameter vector is shown in Table 3.1. The Fourier transforms of C and M, $\tilde{C}(\boldsymbol{\theta};q)$ and $\tilde{M}(\boldsymbol{\theta};q)$ respectively, are then used to construct the charge intensity, I_c and R_m signals ready for fitting to the data as follows (derivation in Appendix A):

$$I_c = |\tilde{C}|^2$$
$$R_m = \frac{|Re(\tilde{M})[\beta\, Re(\tilde{C}) + \alpha\, Im(\tilde{C})] - Im(\tilde{M})[\alpha\, Re(\tilde{C}) + \beta\, Im(\tilde{C})]}{|\tilde{C}|}$$

where *Re* and *Im* are the real and imaginary parts of complex quantities, and α and β are the real and imaginary components of the complex index of refraction for magnetite.

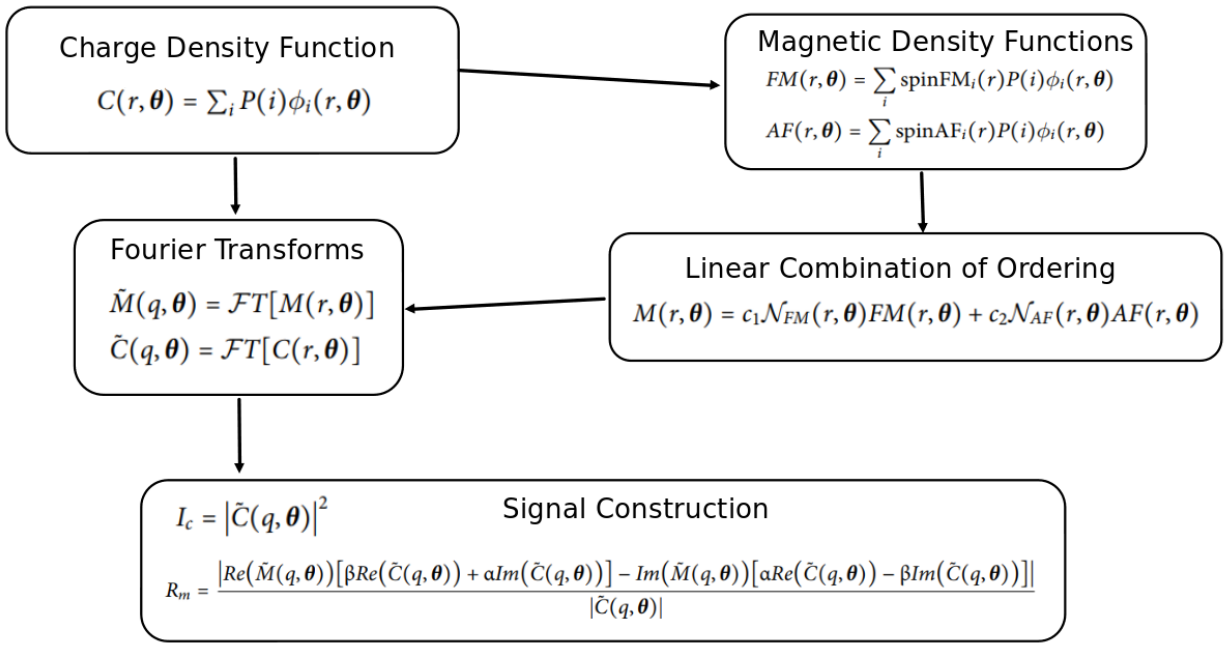

Figure 3.4 Overview of computation flow for the nano chain model beginning at charge density function construction through to signal generation.

3.1.2 Empirical Gaussian Fit

In addition to the real space model discussed above, we also make use of an empirical model composed of a sequence of Gaussian packets to fit the signals I_c and R_m directly to the reciprocal space scattering data and extract values for the correlations and relative amounts of FM and AF ordering present in the samples. This method relies on an examination of the features present in the q-space charge scattering signal $I_c(q)$ and magnetic ratio signal $R_m(q)$. For each sample, both the $I_c(q)$ and $R_m(q)$ signal exhibit a primary peak located near q^*. In the case of $I_c(q)$ this peak corresponds to the average inter-particle distance, and for $R_m(q)$, this peak corresponds to a FM ordering as every particle is aligned with its neighbors. In the case of $I_c(q)$, the position of the peak does not noteably shift at all with the applied field. Because of this, we first use a simple fit of the charge scattering signal to find the value of q^* which then determines the initial value of the FM peak position parameter. Another region of interest in the R_m signal is located around $q^*/2$. This is

Parameter	Description	Constraints
θ_1	Central Amplitude	[0,∞)
θ_2	Central Width	(0,∞)
θ_3	FM Amplitude	(0,∞)
θ_4	FM Width	$(0,\sigma^*)$
θ_5	FM Peak Position	$q^* \pm \varepsilon$
θ_6	AF Amplitude	$\theta_6 < \frac{(1-VSM)\theta_3}{VSM}$
θ_7	AF Width	$(0,\sigma^*)$
θ_8	AF Peak Position	$\frac{q^*}{2} \pm \varepsilon$
θ_9	Baseline Offset	[0,∞)

Table 3.2 Description of the parameters used in the empirical fitting model and their respective constraints. σ^* was chosen to be ~ 0.15 nm^{-1} so that the parameter would not get trapped at extreme values during optimization. ε is about 3% of q^*. VSM is the value for the M/M_s ratios extracted from the VSM data and is used as a normalizing factor.

of note because half the distance of q^* in reciprocal space translates into to a period in real space that is twice as long as the average inter particle spacing and which therefore corresponds to AF ordering. To model the $R_m(q)$ data we then sum the Gaussian functions for FM, AF and random order with a baseline shift as follows:

$$R_m(\boldsymbol{\theta};q) = \frac{\theta_1}{\theta_2\sqrt{2\pi}}\,exp(\frac{-q^2}{2\theta_2^2}) + \frac{\theta_3}{\theta_4\sqrt{2\pi}}\,exp(\frac{-(q-\theta_5)^2}{2\theta_4^2}) + \frac{\theta_6}{\theta_7\sqrt{2\pi}}\,exp(\frac{-(q-\theta_8)^2}{2\theta_7^2}) + \theta_9$$

where the variables are described in detail in Table 3.2

3.2 Parameter Optimization Methods

3.2.1 Levenberg-Marquardt

The Levenberg-Marquardt (LM) algorithm [14, 15] is a robust and efficient method for solving non-linear least squares problems and is generally considered to be the best starting point for non-linear parameter optimization. Broadly speaking the LM algorithm takes best elements of the Gauss-Newton and gradient descent methods by interpolating between the two through the use of a damping coefficient. This work uses the implementation of the LM algorithm found in the LMfit python library [16]

3.2.2 Basin Hopping

One of the significant problems we encountered during the search for best fit parameters was with the LM algorithm falling into local minima rather than the ideal global minimum that we were looking for. The reciprocal space model was particularly vulnerable to local minima because the summation of the variables used often meant there were different combinations of parameter values that yielded the same result. The constraints we imposed on the parameters helped to alleviate this. But we needed to employ a basin hopping algorithm, on top of the LM fitting process, to jostle fit results out of flat or otherwise shallow anomalies in the profile likelihoods for our parameters of interest.

The basin hopping algorithm [17] works by taking the last best fit results and applying a small random perturbation to the parameter values. These new perturbed values are then used as the initial values for a subsequent run the LM fitting process. We used the implementation of basin hopping found in the LMfit python library [16] with the number of iterations set at 200 hops. We found that this value was sufficient to arrive at the global minimum within the constraints.

Chapter 4

Results and Analysis

The great British statistician, George Box, is often attributed with the saying "all models are wrong, but some are useful" [18]. This aphorism points to one of the core concerns at the heart of any modeling process: how reliable are a model's results? Here we examine the results of applying the two models described above and the methods we used to analyze their reliability and quantify their error. We first examine the Fisher information matrix (FIM) associated with the model for a given data point and, when applicable, construct profile likelihoods for our parameters of interest.

4.1 Fisher Information Matrix

The Fisher Information Matrix (FIM) formalism is a method intended to determine how well the model parameters are constrained by the data. A more in-depth discussion of the method and Fisher information in general can be found here [19, 20]. The essence of the technique is that the eigenvectors and eigenvalues of the FIM contain information about how well a model transforms points in parameter space to points in data space. The eigenvectors represent important directions in parameter space, while the eigenvalues associated with each eigenvector give an indication of how relevant that direction is to the model transformation. Eigenvectors with small

eigenvalues correspond to directions, or changes in parameter values, that have lesser effects on the transformation's output. Figure 4.2 shows the difference between the eigensystem of a well constrained model versus one where the model is poorly constrained results and where some parameters could likely be omitted from the model without loss of predictive capability. In the initial iteration of the empirical fit model we used parameters for the FM and AF amplitudes constrained only by the simple bounds of $[0,\infty)$, which led to poorly conditioned FIM results and we found that reparameterizing the AF parameter to include constraints as shown in in table 3.2 improved the eigensystems for the FIM across the data sets.

4.2 Profile Likelihood

The FIM method of determining the error and confidence in the results was generally sufficient for the nano-chain model, but due to the distinct non-linearity of the empirical fitting model we utilized the profile likelihood method to quantify the error ranges for the ratio of AF to FM ordering present in the samples. The profile likelihood method uses the f-test to compare an alternate model to the best fit result and determine to a given confidence value how much of the difference between the two models is the result of a significant change in parameters and not just due to the loss of a degree of freedom.

$$F(P_{fix}, N-P) = (\frac{\chi_f^2}{\chi_0^2} - 1)\frac{N-P}{P_{fix}} \tag{4.1}$$

where χ_0^2 is the residual of the best fit, and χ_f^2 the residual of a test model. Additionally, P_{fix} is the number of fixed parameters in the alternate model, N the number of data points, and P the number of parameters in the best fit model. In our case, for the construction of the profile likelihood we fixed one parameter in the test models, and there are $N = 152$ data points and $P = 9$ parameters in the best fit model, leading to $F(1,143) = 3.907$. Using this value to solve the above equation for χ_f^2 gives us all the models whose parameter result falls within the 95% confidence interval. Figure 4.1

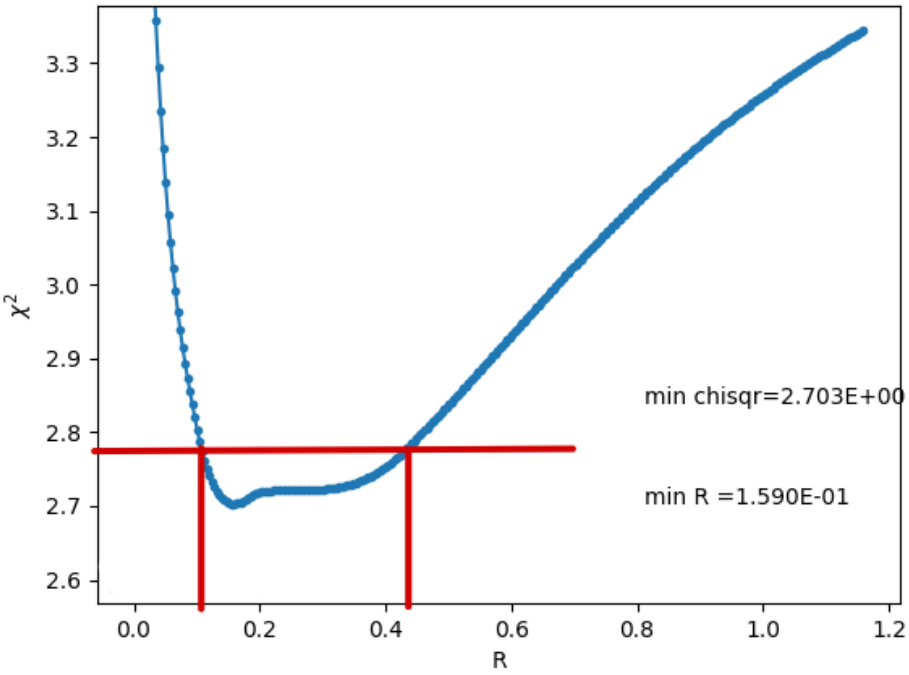

Figure 4.1 Example profile likelihood constructed by fixing the AF/FM ratio and letting the remaining variables freely vary during the parameter optimization. The red horizontal line corresponds to the χ^2_f solution of equation 4.1. The boundaries of the confidence interval is constructed by projecting the intersection points between the red horizontal line and the profile down to the x-axis.

shows the line of demarcation for accepted test models. Where the line intersects with the profile likelihood determines the bounds on the parameter of interest. While the profile likelihood method can yield better results, it is quite computationally expensive to run. Therefore we only constructed the profiles for the main figure of interest.

4.3 Model Results

This work applies the nano chain model to the NP11 sample and uses the FIM to calculate the standard error in the parameters of interest. We also examine how reducible the nanochain model is and what constraints the data imposes upon the transformation from parameter space to data space

using the methods described above. We apply the Gaussian empirical fit to both NP11 (at 20 K, 280 K) and NP5 (at 15 K, 300 K) samples and construct profile likelihood to estimate the confidence intervals.

4.3.1 Nanochain Model

The nanochain model is a mechanistic model and is constructed such that each of the parameters has interpreted meaning. Our evaluation of the FIM eigensystem revealed that four of the original 12 parameters of the nanochain model are poorly constrained by the data. Figure 4.2 shows a comparison of the full model versus the 10-parameter model for sample NP11 at $H = -100$ Oe and at $T = 300$ K. The multitude of very small normalized eigenvalues for the full 12 parameter model indicates that the model is sloppy, and the eigenvectors show us which parameters are poorly constrained. We can see from figure 4.2e that the eigenvectors with the smallest eigenvalues point solely in the direction of the parameters associated with the central peak width for both the charge and magnetic signals which indicates that they are not well constrained by the data. This is not surprising considering that there are no data available in the central $q = 0$ region to directly compare with in the optimization process. The beam stop of the optical setup blocks the detector from picking up any signal in the center of the beam where there would need to be data in order to well constrain the parameters associated with the central peak width in the $I_c(q)$ and $R_m(q)$ signals. The overall results of the nanochain model are displayed in figure 4.3 and show an increase in AF ordering at applied values near remanence. Additionally, table 4.1 collects the magnetic correlations derived from the model parameters.

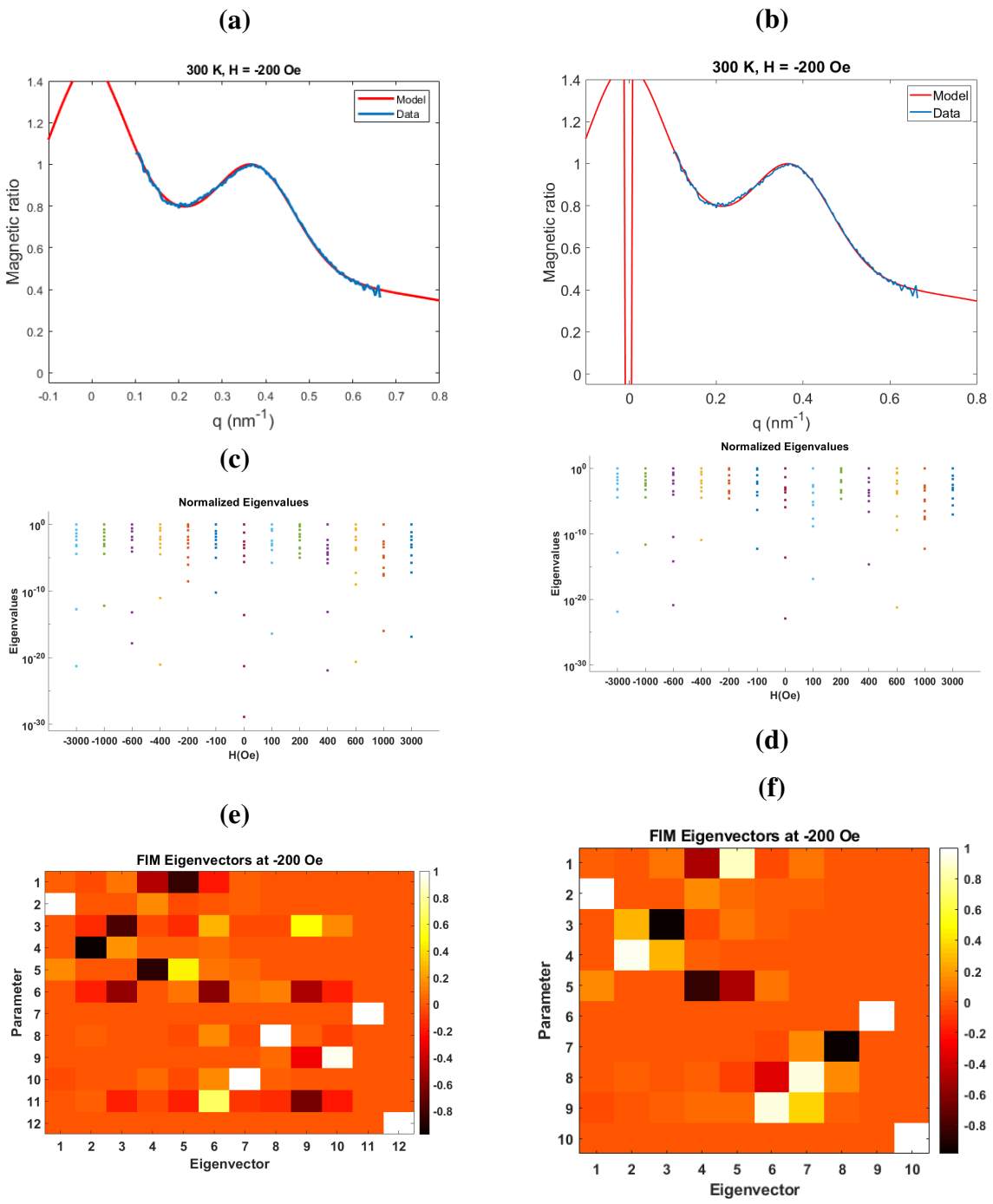

Figure 4.2 Analysis of nanochain model results. (a, b) example fits, (c, d) FIM Eigenvalues, (e, f) and FIM eigenvectors for the full 12 parameter model (left) and the model reduced to 10 parameters (right). The eigenvectors are expressed in the basis of parameters and the color of the grid represent the coefficient of that component. The dip visible in the (b) fit is an artifact of the reduction of parameters and shows that the loss of those parameters does not appreciably affect the fitting region of interest.

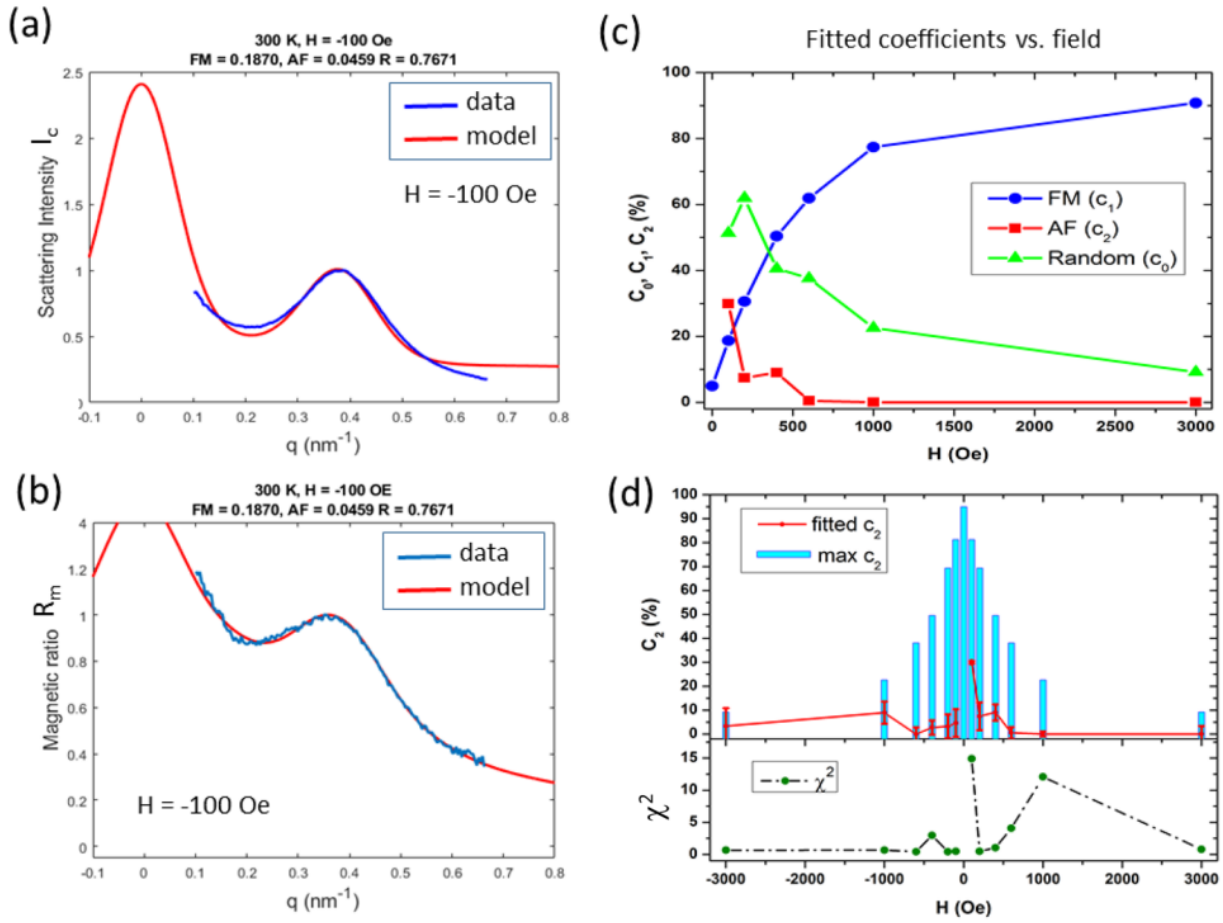

Figure 4.3 Fitting results for the nano chain model. (a-b) Example of fits performed at field $H = -100$ Oe, on (a) the charge scattering intensity I_c data and (b) the magnetic ratio R_m data; (c) Fitted coefficients (expressed as percentages) for the FM component (c_1), the AF component (c_2), and the random component(c_0) as a function of magnetic field H for positive H; (d) Fitted AF coverage (c_2) including error bars at 95% confidence intervals for the whole range of magnetic fields (-3000 Oe, +3000 Oe). The blue bars indicate the possible range for c_2, the maximum value being set by $1 - c_1$ ($c_0 = 0$). Also plotted, the χ^2 values of the LM algorithm. Extracted from [13]

H(Oe)	σ_{FM}(nm)	λ_{FM}(nm)	σ_{AF}(nm)	λ_{AF}(nm)
-3000	18.18	36.87	7.266	14.24
-1000	18.67	37.34	7.244	14.20
-600	17.66	35.32	7.03	13.78
-400	17.25	34.50	7.22	14.15
-200	16.88	33.76	6.95	13.62
-100	15.46	30.92	7.16	14.03
0	20.70	41.40	6.62	12.97

Table 4.1 Listing of the AF and FM correlation lengths (λ_{FM} and λ_{AF}) for the negative branch of the magnetization loop for NP11 at 300 K. The correlation lengths are calculated from the width of the respective Gaussian functions that are used in the real space nanochain model, $\lambda = 2\sqrt{2}\log 2\sigma$.

4.3.2 Empirical Gaussian Fit

We applied the Gaussian fit model to data from both the NP11 and NP5 samples, and found that the FIM are better behaved when a model constrains the ratio of AF and FM parameters, as limited by the VSM measurements. Figures 4.6 and 4.7 illustrate the ratio results for NP5 at 15 K and 300 K and for NP11 at 20 K, and 280 K. The 95% confidence interval at applied fields near remanence show a significant separation and indicate a well defined difference in values. Using these ratios and the VSM data we provide an estimation of the magnetic ordering coefficients displayed in figures 4.4 and 4.5. These coefficient plots indicate a general trend of increased AF ordering at lower field values. But as can be seen by the dip in figure 4.5a at $H = -300$ Oe, the normalization method we utilized causes problems because the M/M_s ratio is very close to zero. Therefore when we multiply the normalization factor it effectively zeroes out the result and causes the erroneous dip in the coefficient. The ratio plots found in figures 4.6 and 4.7 provide a better representation

of the AF predominance at low temperatures and field values. We also see that the larger particle NP11 sample exhibits greater AF ordering than the smaller particle NP5 sample. For NP5 this ratio reaches an average of 1.54 within the 95% confidence interval (CI) $[0.33, 3.01]$, whereas for NP11, it reaches about 3.85 in the CI $[3.18, 5.35]$.

(a) NP5 Coefficients at 300 K

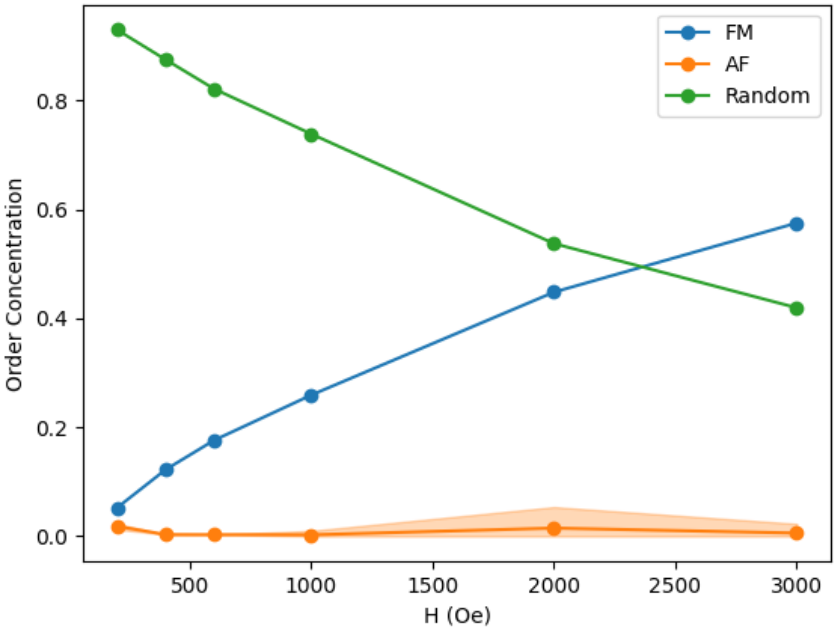

(b) NP5 Coefficients at 15 K

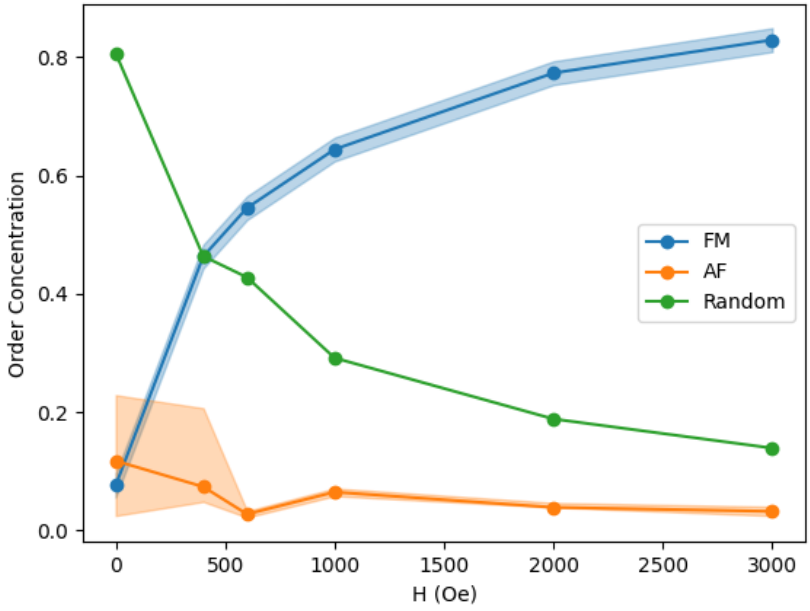

Figure 4.4 Calculated magnetic ordering coefficients for NP5. (a) results for 300 K, and for 15 K (b). Shaded regions representing 95% confidence interval.

(a) NP11 Coefficients at 280 K

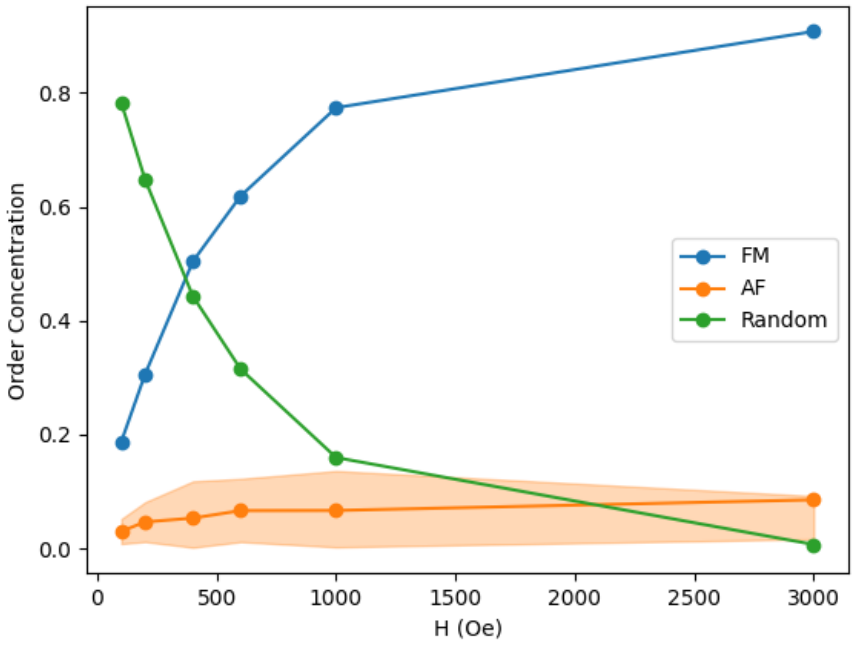

(b) NP11 Coefficients at 20 K

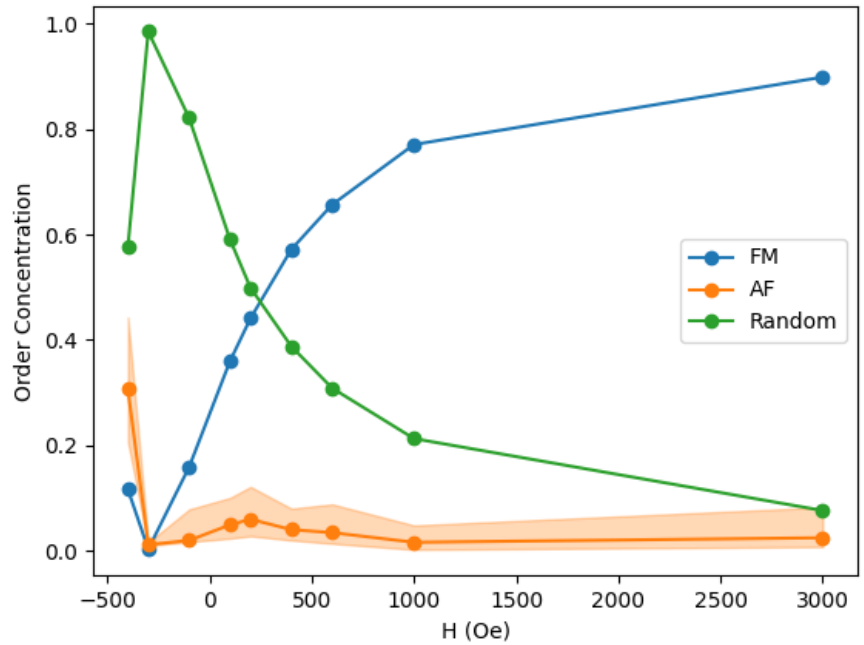

Figure 4.5 Calculated magnetic ordering coefficients for NP11. (a) results for 280 K, and for 20 K (b). Shaded regions representing 95% confidence interval

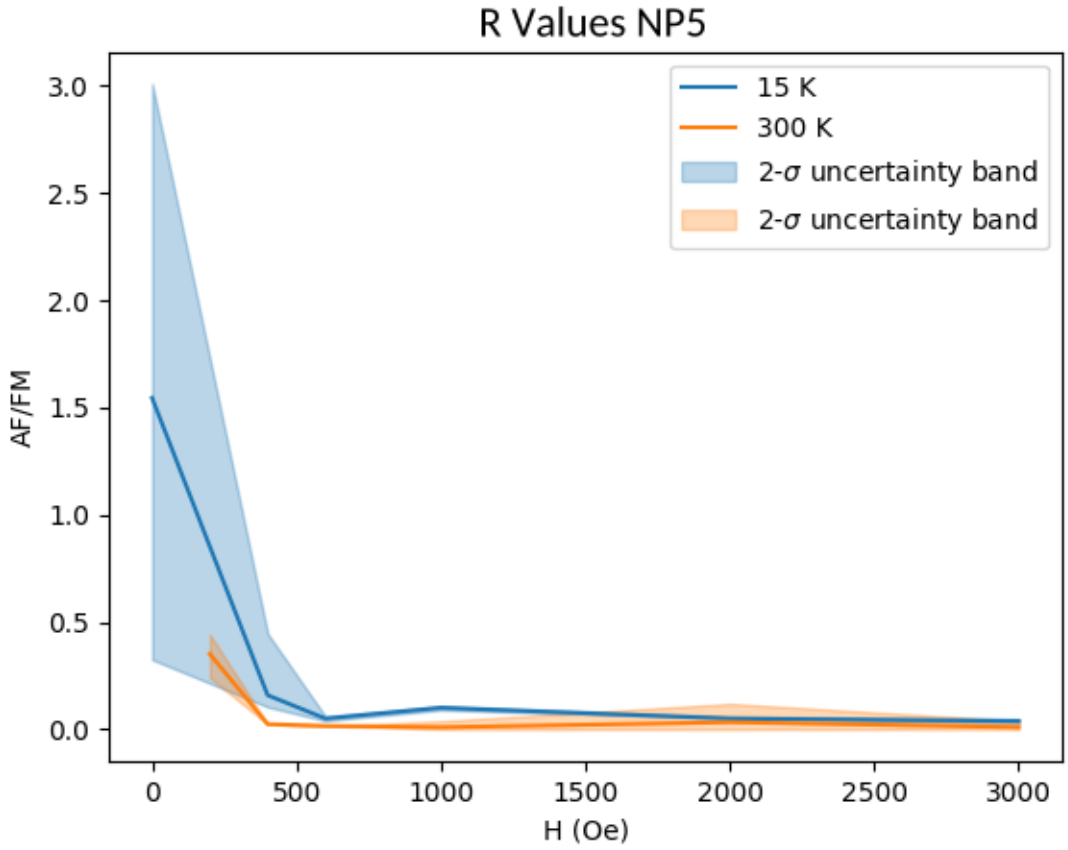

Figure 4.6 Ratio results for the N5 sample at 15 and 300K with shaded region corresponding with the 95% confidence interval for the ratio.

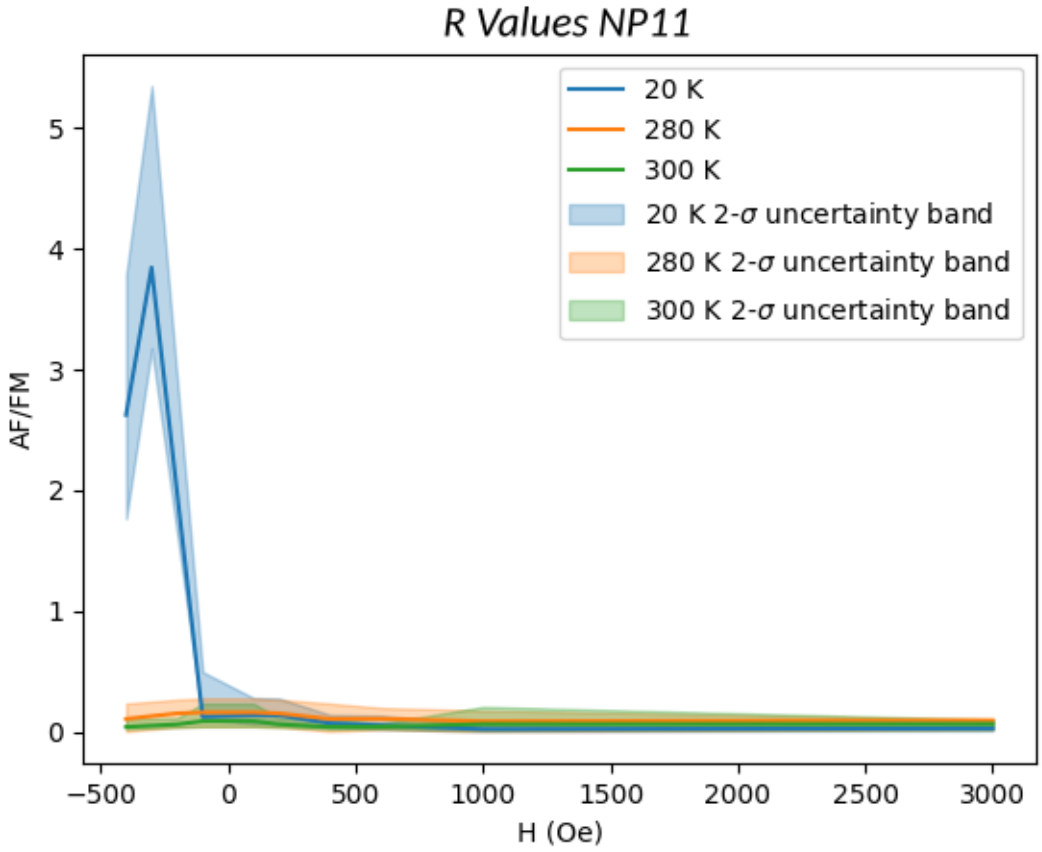

Figure 4.7 Ratio results for the N11 sample at 20 and 280 K and 300 K with shaded region corresponding with the 95% confidence interval for the ratio.

Chapter 5

Conclusion

In this work we have established the validity of computational modeling techniques to probe inter-particle magnetic correlations in assemblies of magnetic NPs using XRMS data. Our modeling of the 11 nm and 5 nm NP assemblies at temperatures above and below their respective blocking temperatures (T_B), shows that when the applied field (H) approaches remanence, the nanospin carried by the individual NPs tends to be randomly oriented though a non-negliable AF contribution is present in the samples at temperatures below the blocking temperature. This behavior is consistent across both the real space nanochain and empirical q-space fitting models and confirmed the superparamagnetic behavior of the material at $T > T_B$. Additionally, it appears that the AF correlations are stronger for the 11 nm NPs compared to the 5 nm with the former's AF/FM ratio 3 times larger.

Further work expanding the nanochain model from a 1D representation, to a 2D model to fit the original 2D speckle patterns should provide greater resolution and certainty in the magnetic ordering and correlations parameters. These methods could also be applied to other magnetic NP assemblies to study the dependence of magnetic correlation on the particle size and concentration during the self-assembly process.

Appendix A

Magnetic Ratio Derivation

X-ray magnetic circular dichroism proves to be an effective tool at extracting the magnetic signal from scattering data. To do this, we use the theory of magnetic scattering where the scattering factor f may be written as

$$f_{\pm} = f_c \pm f_m$$

with f_c and f_m are the charge and magnetic scattering factors respectively with $\pm$ representing the helicity of the circularly polarized light in the plane transverse to propagation.

The scattering amplitude A of a nanoparticle assembly in a given direction q in the scattering space can then be expressed as

$$A_{\pm}(q) = \sum (f_{c,j} \pm f_{m,j}) e^{i\vec{q}\cdot\vec{r}j} = f_c s_c \pm f_m s_m = A_c \pm A_m$$

where the summation indexed by j is over all the atoms. We simplify the expression for the A by introducing a charge and magnetic structure factor, s_c and s_m. These both respectively depend on the spatial distributions of the charge and magnetism in the sample, and are both q dependent. The scattering amplitude A can therefore be written as a sum of the charge and magnetic amplitudes

A_c and A_m. The scattering intensity I observed at the detector is related to the scattering amplitude through

$$I_{\pm} = |A_{\pm}|^2 = |A_c|^2 \pm (A_c A_m^* + A_m A_c^*) + |A_m|^2$$

The scattering intensity is comprised of a pure charge term, $|A_c|^2$, a pure magnetic term, $|A_m|^2$, and a cross term whose sign is dependent on the polarization of incident light. We can exploit the difference polarization has on the scattering to extract the magnetic contribution using a quantity we call "magnetic ratio R_m" (modified from the standard dichroic ratio)

$$R_m = \frac{I_+ - I_-}{\sqrt{I_+ + I_-}}$$

Where I_+ and I_- are the intensities associated with their respective helicities. The magnetic component A_m is typically small with respect to A_c which reduces the dichroic ratio to:

$$R_m = \frac{A_c A_m^* + A_m A_c^*}{\sqrt{|A_c|^2 + |A_m|^2}} \sim \frac{A_c A_m^* + A_m A_c^*}{|A_c|}$$

The numerator can be further reduced but breaking the complex quantities A_c and A_m into their real and imaginary components.

$$f_c = f_{c,1} + i f_{c,2} \text{ and } f_m = f_{m,1} + i f_{m,2}$$

$$s_c = s_{c,1} + i s_{c,2} \text{ and } s_m = s_{m,1} + i s_{m,2}$$

The results of the x-ray absorption spectroscopy (XAS) collected on the magnetite nanoparticles shows that at the energy chosen for our XRMS measurements (the third peak of our observed L_3-Fe

absorption edge), the real part of the magnetic scattering factor tends to vanish. Therefore, we assume that $f_{m,1} \sim 0$ in order to give A_c and A_m the following form

$$
\begin{aligned}
A_c &= (f_{c,1} + i f_{c,2})(s_{c,1} + i s_{c,2}) = (f_{c,1}s_{c,1} - f_{c,2}s_{c,2}) + i(f_{c,2}s_{c,1} + f_{c,1}s_{c,2}) \\
A_c^* &= (f_{c,1}s_{c,1} - f_{c,2}s_{c,2}) + i(f_{c,2}s_{c,1} + f_{c,1}s_{c,2}) \\
A_m &= (f_{m,1} + i f_{m,2})(s_{m,1} + i s_{m,2}) = (f_{m,1}s_{m,1} - f_{m,2}s_{m,2}) + i(f_{m,2}s_{m,1} + f_{m,1}s_{m,2}) \\
A_m^* &= (f_{m,1}s_{c,1} - f_{m,2}s_{c,2}) + i(f_{m,2}s_{c,1} + f_{m,1}s_{m,2})
\end{aligned}
$$

which leads to

$$
\begin{aligned}
A_c A_m^* &= -i f_{m,2}(s_{m,1} - i s_{m,2})[(f_{c,1}s_{c,1} - f_{c,2}s_{c,2}) + i(f_{c,1}s_{c,2} + f_{c,1}s_{c,2})] \\
&= [-f_{m,2}s_{m,2}(f_{c,1}s_{c,1} - f_{c,2}s_{c,2}) + f_{m,2}s_{m,1}(f_{c,2}s_{c,1} + f_{c,1}s_{c,2})] \\
&+ i[-f_{m,2}s_{m,1}(f_{c,1}s_{c,1} - f_{c,2}s_{c,2}) - f_{m,2}s_{m,1}(f_{c,2}s_{c,1} + f_{c,1}s_{c,2})]
\end{aligned}
$$

and

$$
A_c A_m^* + A_m A_c^* = 2Re(A_c A_m^*) = 2[-f_{m,2}s_{m,2}(f_{c,1}s_{c,1} - f_{c,2}s_{c,2}) + f_{m,2}s_{m,1}(f_{c,2}s_{c,1} + f_{c,1}s_{c,2})]
$$

resulting in

$$
R_m \approx \frac{2f_{m,2}[s_{m,1}(f_{c,2}s_{c,1} + f_{c,1}s_{c,2}) - s_{m,2}(f_{c,1}s_{c,1} + f_{c,2}s_{c,2})}{|f_c||s_c|}
$$

The coefficients $f_{c,1}$, $f_{c,2}$ and f_m are estimated with the XAS data using Kramer-Kronig transformations. $s_{c,1}$, $s_{c,2}$, $s_{m,1}$, $s_{m,2}$ are calculated with the Fourier transforms that are part of our model for the charge density function, and magnetic density functions in a chain of Fe_3O_4 NPs. All these quantities depend on the scattering vector q, so R_m does as well. In the end the modeled $R_m(q)$ and the experimental $R_m(q)$ are compared and various parameters in the model are adjusted to make the model match the experiment. In this process, the quantities $s_{c,1}$, $s_{c,2}$ (and the resulting $|s_c|$) are

concurrently evaluated by fitting the experimental charge scattering intensity:

$$(I_+ + I_-)(q) = |A_c|^2 + |A_m|^2 \approx |A_c|^2 = |f_c|^2 |s_c|^2$$

Once the charge structural factors $s_{c,1}$, and $s_{c,2}$ are adjusted, the magnetic structural factors $s_{m,1}$, and $s_{m,2}$ are adjusted by fitting $R_m(q)$. A weight for the various magnetic components (FM, AF, and random) is then evaluated as well as their respective correlation lengths.

Derivation courtesy of Dr. Karine Chesnel, and published in part in [12]

Bibliography

[1] N. A. Frey, S. Peng, K. Cheng, and S. Sun, "Magnetic nanoparticles: synthesis, functionalization, and applications in bioimaging and magnetic energy storage," Chem. Soc. Rev. **38,** 2532–2542 (2009).

[2] S. Mornet, S. Vasseur, F. Grasset, and E. Duguet, "Magnetic nanoparticle design for medical diagnosis and therapy," J. Mater. Chem. **14,** 2161–2175 (2004).

[3] E. Duguet, S. Vasseur, S. Mornet, and J.-M. Devoisselle, "Magnetic nanoparticles and their applications in medicine," Future Medicine (2006).

[4] J. Gao, H. Gu, and B. Xu, "Multifunctional magnetic nanoparticles: design, synthesis, and biomedical applications," Accounts of chemical research **42,** 1097–1107 (2009).

[5] J.-S. Lee, J. Cho, C. Lee, I. Kim, J. Park, Y.-M. Kim, H. Shin, J. Lee, and F. Caruso, "Layer-by-layer assembled charge-trap memory devices with adjustable electronic properties," Nature nanotechnology **2,** 790–795 (2007).

[6] S. Chemicals, "Automotive Applications of Nanomaterials," .

[7] L. Blaney, "Magnetite (Fe3O4): Properties, synthesis, and applications," (2007).

[8] Y. Cai *et al.*, "Orbital and spin moments of 5 to 11 nm Fe3O4 nanoparticles measured via x-ray magnetic circular dichroism," Journal of Applied Physics **115,** 17B537 (2014).

[9] K. Chesnel, J. Nelson, B. Wilcken, and S. D. Kevan, "Mapping spatial and field dependence of magnetic domain memory by soft X-ray speckle metrology," Journal of Synchrotron Radiation **19,** 293–306 (2012).

[10] K. Chesnel, M. Trevino, Y. Cai, J. M. Hancock, S. J. Smith, and R. G. Harrison, "Particle size effects on the magnetic behaviour of 5 to 11 nm Fe3O4 nanoparticles coated with oleic acid," Journal of Physics: Conference Series **521,** 012004 (2014).

[11] S. Klomp *et al.*, "Size-Dependent Crystalline and Magnetic Properties of 5–100 nm Fe3O4 Nanoparticles: Superparamagnetism, Verwey Transition, and FeO–Fe3O4 Core–Shell Formation," IEEE Transactions on Magnetics **56,** 1–9 (2020).

[12] K. Chesnel *et al.*, "Unraveling Nanoscale Magnetic Ordering in Fe3O4 Nanoparticle Assemblies via X-rays," Magnetochemistry 4 (2018).

[13] J. Rackham, B. Newbold, S. Kotter, D. Smith, D. Griner, R. Harrison, A. H. Reid, M. Transtrum, and K. Chesnel, "Modeling inter-particle magnetic correlations in magnetite nanoparticle assemblies using x-ray magnetic scattering data," AIP Advances **9,** 035033 (2019).

[14] K. Levenberg, Quartly of Applied Mathematics 2(1944), 164-168 .

[15] D. W. Marquardt, "An Algorithm for Least-Squares Estimation of Nonlinear Parameters," Journal of the Society for Industrial and Applied Mathematics **11,** 431–441 (1963).

[16] M. Newville, R. Otten, A. Nelson, A. Ingargiola, T. Stensitzki, D. Allan, A. Fox, and F. Carter, "lmfit-py https://zenodo.org/record/5570790," .

[17] D. J. P. K. Wales D J, "Global Optimization by Basin-Hopping and the Lowest Energy Structures of Lennard-Jones Clusters Containing up to 110 Atoms," Journal of Physical Chemistry A, 101, 5111 (1997).

[18] G. E. P. Box, "Science and Statistics," Journal of the American Statistical Association **71,** 791–799 (1976).

[19] M. K. Transtrum, B. B. Machta, and J. P. Sethna, "Why are Nonlinear Fits to Data so Challenging?," Phys. Rev. Lett. **104,** 060201 (2010).

[20] R. Chachra, M. K. Transtrum, and J. P. Sethna, "Comment on "Sloppy models, parameter uncertainty, and the role of experimental design"," Mol. BioSyst. **7,** 2522–2522 (2011).